OPEN

3D Acoustic Wave Sparsely Activated Localization Microscopy With Phase Change Contrast Agents

Kai Riemer, PhD, Qingyuan Tan, MSc, Sophie Morse, PhD, Luca Bau, PhD, Matthieu Toulemonde, PhD, Jipeng Yan, PhD, Jingwen Zhu, MSc, Bingxue Wang, MSc, Laura Taylor, MSc, Marcelo Lerendegui, MSc, Qiang Wu, PhD, Eleanor Stride, PhD, Christopher Dunsby, PhD, Peter D. Weinberg, PhD, and Meng-Xing Tang, PhD

Objective: The aim of this study is to demonstrate 3-dimensional (3D) acoustic wave sparsely activated localization microscopy (AWSALM) of microvascular flow in vivo using phase change contrast agents (PCCAs).

Materials and Methods: Three-dimensional AWSALM using acoustically activable PCCAs was evaluated on a crossed tube microflow phantom, the kidney of New Zealand White rabbits, and the brain of C57BL/6J mice through intact skull. A mixture of C_3F_8 and C_4F_{10} low-boiling-point fluorocarbon gas was used to generate PCCAs with an appropriate activation pressure. A multiplexed 8-MHz matrix array connected to a 256-channel ultrasound research platform was used for transmitting activation and imaging ultrasound pulses and recording echoes. The in vitro and in vivo echo data were subsequently beamformed and processed using a set of customized algorithms for generating 3D super-resolution ultrasound images through localizing and tracking activated contrast agents.

Results: With 3D AWSALM, the acoustic activation of PCCAs can be controlled both spatially and temporally, enabling contrast on demand and capable of revealing 3D microvascular connectivity. The spatial resolution of the 3D AWSALM images measured using Fourier shell correlation is 64 μm, presenting a 9-time improvement compared with the point spread function and 1.5 times compared with half the wavelength. Compared with the microbubble-based approach, more signals were localized in the microvasculature at similar concentrations while retaining sparsity and longer tracks in larger vessels. Transcranial imaging was demonstrated as a proof of principle of PCCA activation in the mouse brain with 3D AWSALM.

Conclusions: Three-dimensional AWSALM generates volumetric ultrasound super-resolution microvascular images in vivo with spatiotemporal selectivity and enhanced microvascular penetration.

Key Words: phase change contrast agents, PCCA, low-boiling point, acoustic vaporization, droplet activation, microcirculation, super-resolution ultrasound, ultrasound localization microscopy, ULM

(*Invest Radiol* 2024;59: 379–390)

Received for publication June 6, 2023; and accepted for publication, after revision, August 19, 2023.

From the Department of Bioengineering, Imperial College London, London, United Kingdom (K.R., Q.T., S.M., M.T., J.Y., J.Z., B.W., L.T., M.L., P.D.W., M.-X.T.); NDORMS, University of Oxford, Oxford, United Kingdom (L.B., Q.W., E.S.); and Department of Physics, Imperial College London, London, United Kingdom (C.D.).

Conflicts of interest and sources of funding: This work was funded in part by the Engineering and Physical Sciences Research Council (EPSRC) under grant EP/T008970/1, EP/T008067/1, and EP/N026942/1; the EPSRC Impact Acceleration Account under grant EP/R511547/1; the National Institute for Health Research i4i under grant NIHR200972; and the British Heart Foundation under grant PG/18/48/33832. The authors report no conflicts of interest.

Correspondence to: Meng-Xing Tang, PhD, Department of Bioengineering, Imperial College London, SW7 2AZ, London, United Kingdom. E-mail: mengxing.tang@ic.ac.uk.

Supplemental digital contents are available for this article. Direct URL citations appear in the printed text and are provided in the HTML and PDF versions of this article on the journal's Web site (www.investigativeradiology.com).

ISSN: 0020-9996/24/5905–0379
DOI: 10.1097/RLI.0000000000001033

Ultrasound localization microscopy (ULM), also known as super-resolution ultrasound, uses super-resolution imaging techniques to track the movement of subwavelength acoustic scatterers between consecutive image frames. Ultrasound localization microscopy offers a spatial resolution several fold higher than that of conventional diffraction limited ultrasound[1] and can visualize key features of the microcirculation such as tortuosity.[2,3] This intricate view of the microvasculature allows observation of disease development, unlike other imaging modalities.[4,5] This includes the detection and characterization of tumors, the diagnosis of cardiovascular disease, and the monitoring of the brain and ophthalmic assessment.[6–11] Ultrasound localization microscopy has been used to identify subtle changes in the tissue microstructure associated with pathogenesis, such as alterations in vascularity and blood volume.[9,12–14] These changes are difficult or impossible to detect using traditional imaging methods.

To date, most ULM studies have used coated gas microbubbles (MBs) as the contrast agent with a diameter between 1 and 10 μm. Microbubbles are medically approved, already used in conventional ultrasound imaging, and provide a very high signal-to-noise ratio. This makes it easy to localize them in a sequence of ultrasound images. The main disadvantage of using MBs is a lack of control over their spatiotemporal distribution. To accurately localize MBs, they must be spatially isolated. Unfortunately, however, MBs follow contrast-enhanced perfusion kinetics. Their signal peaks shortly after a bolus injection and then decays exponentially. In larger vessels (>1 mm), the MB concentration may be too high, causing tracking errors and nonlinear propagation artifacts.[15,16] It is therefore necessary to wait for the bolus to become diluted by dispersion and partial clearance, to deliberately destroy MBs with a high amplitude pulse, to infuse MB at a steady rate, or to use a different flow tracking technique. However, even a constant perfusion rate at a low concentration does not solve the problem that most microvessels do not contain MBs.[17] This leads to very long acquisition times being required to achieve the impressive vascular detail. Phase change contrast agents (PCCAs or nanodroplets [NDs]) 10–1000 nm in diameter of volatile liquid perfluorocarbons can provide benefits over MBs.[18–20] In their liquid state, PCCAs do not scatter ultrasound at medical imaging frequencies. Upon exposure to ultrasound, some PCCAs will vaporize to form a sparse population of echogenic MBs. Because of this and their small diameter, PCCAs can be injected in higher concentrations and can permeate the vasculature at a faster rate.[19,20] Phase change contrast agents can also circulate for longer in vivo,[19] allowing for an even distribution in the vasculature and providing flexibility as to where and when the contrast-enhanced signal is generated.[21]

The benefit of selective ULM with acoustically activated PCCAs, which we termed acoustic wave sparsely activated localization microscopy (AWSALM),[21,22] is limited if imaging is performed 2-dimensional (2D). Unlike MB-based ULM, a disadvantage of the selectivity of AWSALM is that activation has to occur within the field of view of the transducer. A 1D linear array can only activate PCCAs in a plane beneath. Microvascular structures are complex and 3D, and the feeding vessel may lie in a

different plane from the microvasculature. To fully control the contrast in a volume of interest, activation in 3D is necessary. Recent demonstrations of 3D ULM with MBs have shown unprecedented detail and diagnostic value for imaging in tumors, the heart, or in the brain.[23–27] Imaging acoustically activated PCCAs in 3 dimensions, however, has not been described before.

In this study, we demonstrate 3D AWSALM with selective PCCA activation anywhere in the volume of interest. We developed an imaging and activation sequence requiring just 256 elements and combined it with perfluorocarbon mixture PCCAs, demonstrating 3D super-resolution generated from PCCAs in a phantom, a rabbit kidney, and a mouse brain. In the following, we first discuss our imaging and activation sequence and present the data processing pipeline. Next, we illustrate the deliberate activation of PCCAs in 2 crossed tubes and show a super-resolved rabbit kidney, in which the selective activation revealed vascular connectivity and increased microvascular localization density. We then compare PCCA activation with 3 different concentrations of MBs from a bolus injection. Finally, we present the feasibility of 3D AWSALM for transcranial imaging and discuss limitations and future work.

MATERIALS AND METHODS

Preparation of Phase-Change Contrast Agents

Three low-boiling-point perfluorocarbon mixture phase change PCCAs with different gas ratios were made as illustrated in Figure 1. Mixing of gases allows low ultrasound pressures to be used to vaporize PCCAs.[21,28] The PCCAs were generated through condensation of phospholipid-coated MBs containing a volume mixture of 2 gases (F2 Chemicals Ltd, United Kingdom): OFP (C_3F_8; boiling point, −36.7°C) and DFB (C_4F_{10}; boiling point, −1.9°C). First, a phospholipid suspension was prepared by mixing 1,2-distearoyl-sn-glycero-3-phosphocholine (DSPC) and 1,2-distearoyl-sn-glycero-3-phosphoethanolamine-*N*-[methoxy(polyethyleneglycol)-2000] (DSPE-PEG-2000) (9:1 molar ratio) in phosphate-buffered saline, propylene glycol, and glycerol (16:3:1 by volume) for a total lipid concentration of 1 mg/mL. Subsequently, 1 mL of the solution was added to a 2-mL glass vial. The head space of the vial was filled with a gas mixture, which was prepared by filling a 20-mL syringe with C_3F_8 and C_4F_{10} at a fill pressure of 0.3 bar as illustrated in Figure 1. The syringe plunger was set to 0 mL. The 3-way tap (TWT) numbered (I) in Figure 1 connected either gas cylinder to the TWT numbered (II) as marked by the black arrow. The TWT (II) connected TWT (I) to the syringe (green arrow) or to a free flow outlet (red arrow). The default position connected a gas cylinder to the syringe (black to green). The syringe plunger was driven outward by being filled from 1 of the cylinders, using a pressure of 0.3 bar, until a desired volume was reached. TWT (I) was then turned to connect the other cylinder to the syringe until 20 mL was reached. Detached from this setup, the syringe with a gas volume ratio of 4:1, 3:1, or 1:1 was used to fill the headspace of the vial. Via two 21-gauge needles, the air in the headspace of the vial was exchanged with the gas mixture from the syringe. One needle was connected to the syringe and pushed into the vial through the rubber sealing. Another needle was pushed into the rubber sealing as a free flow outlet. The syringe plunger was pushed fully to ensure a complete exchange. The syringe size and fill pressure were optimized to slow down the mixing process, ensuring maximum repeatability; the syringe plunger was pushed at a rate of approximately 0.5 mL/s. The higher the ratio of C_3F_8, the lower the energy required for activation. A minimum of 10 minutes was allowed for the gases to mix. Next, MBs were generated through 90 seconds of mechanical agitation with a TP-103 amalgamator (Goldsmith Reverse, United States). The MB vial was submerged in a −10°C water-salt solution for 10 minutes. Finally, MBs were transformed into phase changing PCCAs through condensation by compressing the cooled solution inside a 1-mL syringe until it becomes transparent. The PCCA diameters ranged from 10 to 1000 nm with a mean value of 119 nm based on prior measurement[22] using a NanoSight NS300 (Malvern Instruments Ltd, United Kingdom). The average number of MBs and NDs per milliliter was 5.5×10^9 and 6×10^9, respectively.[29] For up to 30 minutes, droplets from a single vial were used in experiments after which a new vial was prepared. The gas ratio was changed according to the imaging subject of interest (crossed tubes, 1:1; rabbit kidney; 3:1; mouse brain, 4:1).

Experimental Setup

In this study, we used 4 experimental setups in 3 imaging subjects as illustrated in Figure 2 and defined 9 aims (i–ix). All experiments complied with the Animals (Scientific Procedures) Act 1986

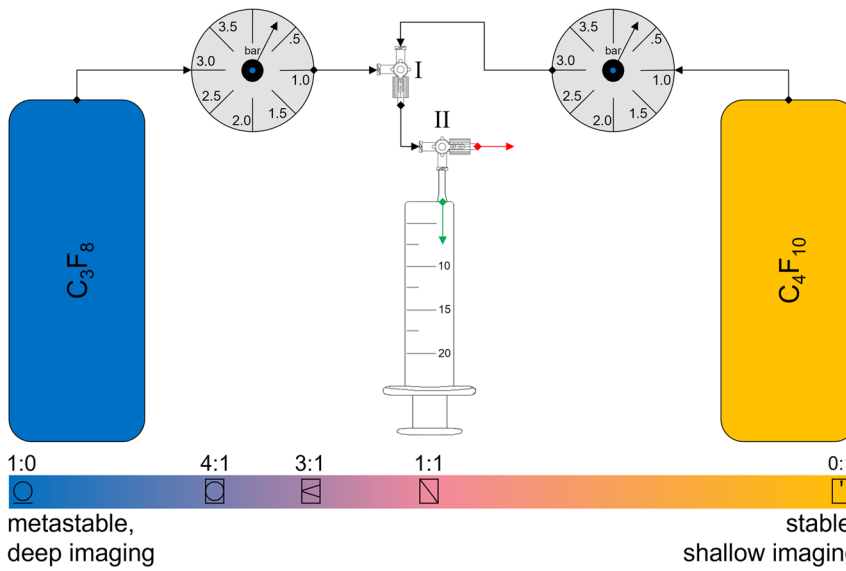

FIGURE 1. Gas mixing procedure by volume with same fill pressure through the use of a gastight syringe and multiple 3-way switches. The composition of the gas mixture dictates the characteristics of PCCAs (stable to metastable). The syringe was filled with 4, 5, or 10 mL of C_3F_8, the 3 way switches were rotated, and the remaining volume was filled with C_4F_{10}. The gas ratio was changed according to the imaging subject of interest. Crossed tubes, 1:1; rabbit kidney, 3:1; mouse brain, 4:1.

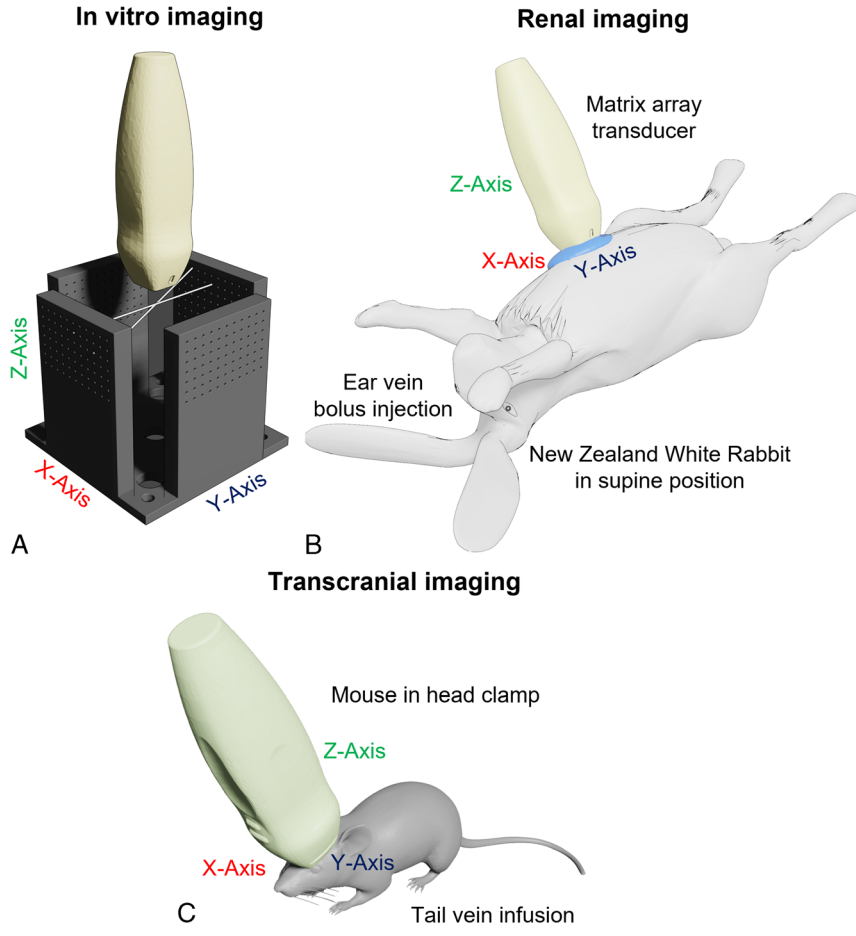

FIGURE 2. Four experimental setups in 3 imaging subjects (A) in vitro imaging of 2 crossed tubes, (B) renal imaging of a NZW rabbit and comparison between 3D MB ULM and 3D AWSALM in the rabbit kidney, and (C) transcranial imaging of a mouse.

and were approved by the Animal Welfare and Ethical Review Body of Imperial College London.

Two Crossed Tubes Phantom

Two intersecting cellulose tubes with 200 μm inner and 300 μm outer diameter as illustrated in Figure 2A were used for validation of (i) deliberate activation of PCCAs, (ii) selective activation of either tube, and (iii) separation of 2 structures below the full width at half maximum of the system's PSF. The tubes were submerged in water heated to 37.5° ±0.5°C, connected to a programmable PHD2000 syringe pump (Harvard Apparatus, United States), the volume flow rate was 20 μL/min, and the PCCA concentration was 3×10^3 ND/mL. Both tubes were perfused with PCCA at all times.

Renal Vasculature of Rabbit

To show the activation of PCCAs (iv) in vivo, (v) to visualize the selective activation in different regions of the renal vasculature, and (vi) to demonstrate microvascular connectivity, imaging was performed on the left kidney of anesthetized specific pathogen-free male New Zealand White (NZW) rabbits as illustrated in Figures 2B. A total of 6 rabbits (HSDIF strain; mean age, 17.67 weeks; mean weight, 2.98 kg; Envigo, United Kingdom) were used. The rabbits were sedated with acepromazine (0.5 mg/kg, intramuscular) and anesthetized with 1 dose of medetomidine (Domitor, 0.25 mL/kg, intramuscular) and ketamine (Narketan, 0.15 mL/kg, intramuscular). Every 30 minutes, a third of the initial dose (acepromazine and medetomidine) was administered for a maximum duration of 4 hours. Via the marginal ear vein, PCCAs were injected. The first injection was 0.1 mL, each subsequent injection was either 0.05 or 0.1 mL of undiluted PCCAs. For euthanasia, pentobarbital (0.8 mL/kg) was used. The rabbits were shaved, positioned supine, kept warm with a heated mat, and ventilated at 40 breaths per minute. Heart rate and blood oxygen saturation were monitored continuously.

Comparison Between 3D MB ULM and 3D AWSALM

To illustrate (vii) the benefits of PCCAs for microvascular imaging and (viii) to demonstrate limitations of either the same setup as shown in Figure 2B was used. Microbubbles were injected as a bolus of 0.1 mL. After injection, images were acquired every 30 seconds for a total of 8 minutes to investigate different MB concentrations. We waited 5 minutes between the last MB and first PCCA acquisition and visually confirmed all MBs washed out. The imaging script was kept the same between MB and PCCA (except focus sequence disabled).

Feasibility of Transcranial Imaging of a Mouse Brain

To demonstrate (ix) the feasibility of 3D transcranial AWSALM, imaging was performed on 2 female mice (C57BL/6J strain; mean age, 6 months; mean weight, 34.8 g; Envigo, United Kingdom) as illustrated in Figures 2C. Undiluted PCCAs were injected via the tail vein at 20 μL/min using the programmable PHD2000 syringe pump. Note, that

the degree of spontaneous vaporization was high due to the large percentage of C_3F_8 as can be seen in the Supplementary Video 4, http://links.lww.com/RLI/A873. The fur above the skull was removed with depilatory cream. Anesthesia was maintained with an anesthetic vaporizer (Harvard Apparatus, England) through breathing of 1.5%–2.0% vaporized isoflurane (Zoetis, United Kingdom) mixed with oxygen (0.8 L/min). A total of 15,000 frames from 10 acquisitions were used to map the brain vasculature.

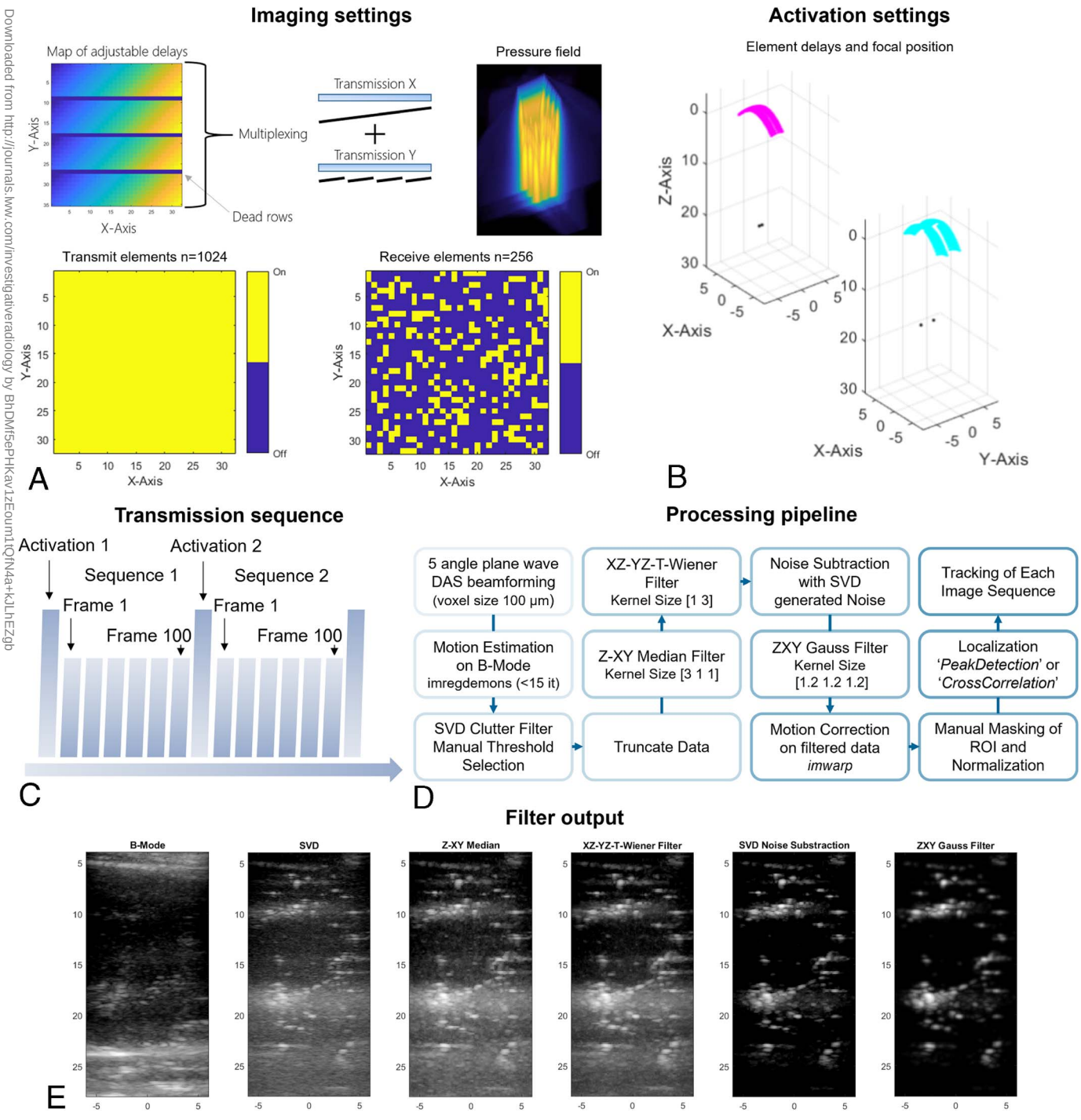

FIGURE 3. Detailed 3D AWSALM super-resolution image generation schematic of (A) imaging and (B) activation settings, (C) transmission sequence of plane wave and focused transmissions, (D) data processing pipeline, and (E) exemplary result of each successive processing step on the maximum projection along the X-direction of a single time point. A, This exact set of 256 elements was used in reception to generate contrast-enhanced volumes. B, The activation sequence was adjusted according to real-time feedback and differed between all acquisitions. Image illustrates 2 possible settings of how focusing was achieved using a subaperture of multiple lines with different depth and X-Y-position. E, The B-mode and SVD image are shown with a dynamic range of 40 dB, all other images are shown with a dynamic range between 0 and 1.

Ultrasound Scanner

A multiplexed Vermon 8-MHz matrix array (Vermon, France) and a Verasonics Vantage 256 ultrasound research platform (Verasonics, United States) were used for the experiments. The mechanical index (MI) was derated based on an attenuation coefficient $\alpha = 0.3$ db/(MHz · cm) and calibrated in a water tank with a 0.2-mm needle hydrophone (Precision Acoustics, United Kingdom). To determine a representative MI with a focused transmission, a focal depth of 22 mm was selected. The hydrophone was placed in the middle of the probe, and all elements in a line were used to focus. To determine the point spread function (PSF) of the system and its resolution, a wire target was used and imaged both in the X- and Y-direction. The wire target was positioned at 5 different XYZ locations, and the average full width at half maximum of the wire target was used (593 μm) to use as reference for the resolution improvement.

3D AWSALM: Imaging and Activation Sequence

In 3D AWSALM, the ultrasound transmissions for PCCA activation and imaging were separate from each other and interleaved as illustrated in Figure 3C. For each activation, 100 imaging frames were acquired. The imaging sequence consisted of 5 single-cycle plane waves at −6, 0, 6 degrees and −6, 6 degrees in the X- and Y-directions, respectively. In transmission all and in reception a randomly selected set of 256 elements as illustrated in Figure 3A were used. In transmission, a replication of the transmit pulse on 4 separate subapertures was achieved by multiplexing. The random selection was performed once and kept the same for all acquisitions as illustrated. A pulse center frequency ($TX_{img} = 8$ MHz), an MI ($MI < 0.08$), and a frame rate ($FR = 200$ Hz) were used. For the activation of PCCAs, 10 half cycles were transmitted at a center frequency ($TX_{foc} = 5$ MHz), with an MI ($MI < 0.15$) and a frame rate ($FR = 50$ Hz). This was combined with a variable number of focal positions, variable number of elements, and variable number of transmissions as illustrated in Figure 3. Each sequence was repeated 15 times. Before the first activation sequence, 100 frames were acquired, and after each activation, 100 frames were captured for a total of 1600 frames. The focus position was manually selected within the region of interest (ROI) between the top/upper left corner (−5/−5/0 mm) and the bottom/lower right corner (5/5/30 mm). The number of elements used ranged between 2 and 32 rows each with 8–32 elements. The number of transmissions was selected between 2 and 15, and the total acquisition time was <9 seconds (activation and imaging).

Data Processing

The data processing pipeline and the output of each processing step are illustrated in Figures 3D and E. Each sequence of images (100 frames) was processed individually in MATLAB (vR2021a; MathWorks, United

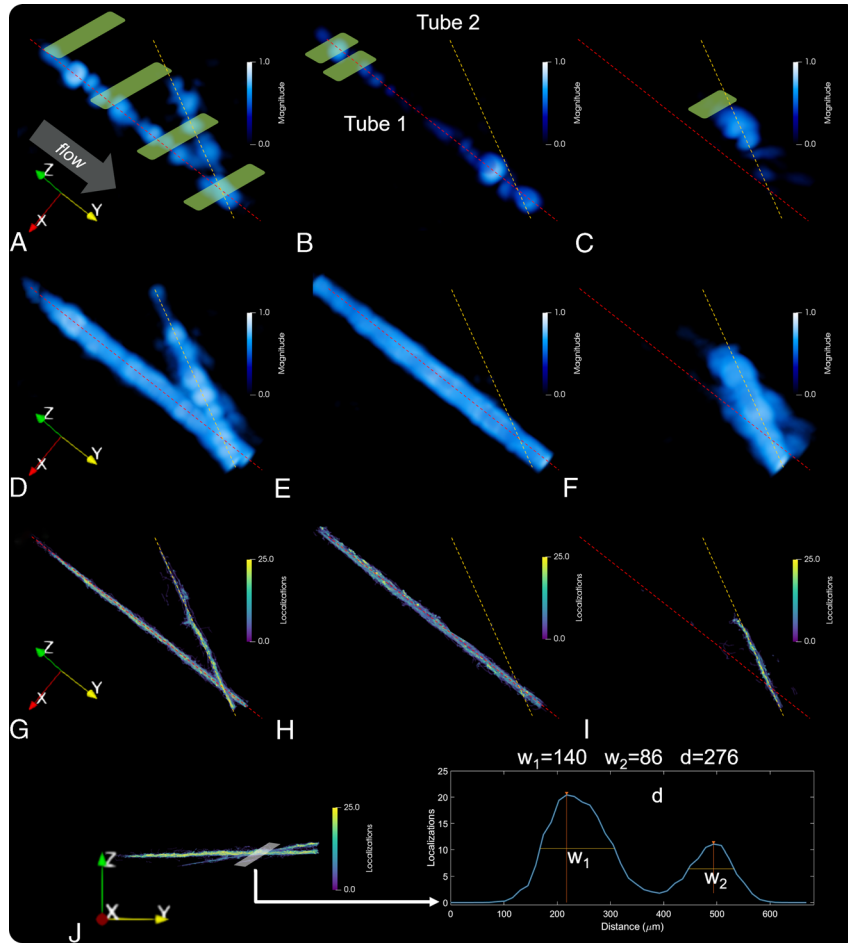

FIGURE 4. Activation of PCCAs in a phantom with 2 crossed tubes. Tube 1 is highlighted with a red dashed line and tube 2 with an orange dashed line. A–C, Illustrate a single time point with activation of PCCAs in (A) both tubes, (B) tube 1, and (C) tube 2. The locations of the activation foci are indicated by the green rectangular regions. Maximum projection of (A, B, C) over all time points is shown in (D, E, F) and super-localized maps in (G, H, I), respectively. Using the data from (A/D), a plot of localization density (J) averaged over the width indicated by the white box (left) demonstrates that the tubes can be separated from each other (right).

States). After data acquisition, motion estimation was performed on the B-Mode data. A single reference image was stored from the first sequence for all following sequences for motion estimation. Clutter was removed using singular value decomposition (SVD) and a manually selected threshold. The data were log compressed, truncated, and normalized. A Z-XY median filter and a XZ-YZ-T Wiener filter were applied. The SVD-generated noise was subtracted from the data by generating a noise field from the highest ranked 20% of singular values. This was done as follows: the highest ranked 20% of singular values were used to reconstruct a noise matrix A_{noise}. The temporal mean of the noise matrix A_{noise} was shuffled in X-Y direction and Gaussian blurred. The noise level over time was then estimated, and the matrix multiplied by the noise level factor κ was subtracted from the data ($A_{data} = A_{data} - \kappa \cdot A_{noise}$). Data were ZXY Gaussian blurred, motion was corrected, and a mask was selected manually. The first frame of each sequence was set to 0 so as to not track signals from 2 separate sequences.

Super-Resolution Algorithm

Localization of the contrast signal was done through peak detection (Figs. 3–6) or through 3D normalized cross-correlation (Fig. 7). For cross-correlation, the system's PSF was determined by manual segmentation of up to 10 isolated contrast signals. A patch with size $5 \times 5 \times 5$ voxel centered at each peak of the cross-correlation coefficient/peak detection map was resized with 4 times denser voxel resolution using cubic interpolation. The location was determined by the maximum in each interpolated patch. Localizations in 2 consecutive frames were paired by finding a total cost minimum via a graph-based assignment, and the cost of pairing 2 localizations was defined by the inverse probability obtained from a linear Kalman motion model.[30] A fuzzy initialization method was incorporated to estimate velocity for new localizations to further improve the tracking performance.[10] To minimize human bias in tuning the parameters of the Kalman motion model, the covariance of observation noise was set by the estimated localization uncertainty, and the covariance of prediction noise was estimated from the data. Localizations that were detected to exist for less than 4 frames were excluded from plotting the final ULM maps. The maximum velocity was set between 150 and 250 mm/s. Only the 1500 frames after the first activation were used for ULM processing. Data visualization was done in Matlab or ParaView (v5.11.0, Kitware Inc, United States) through conversion to a VTK file. The Fourier shell correlation (FSC) algorithm[31] and the associated code, which is available on GitHub (https://github.com/bionanoimaging/cellSTORM-MATLAB), was used to evaluate the resolution of localizations. Localized events were divided into 2 groups based on whether they occurred in the even or odd frames. Each group of events was accumulated at their respective localized positions in a separate 3D matrix having cubic voxels of 25 μm in size. The FSC was performed between the 2 matrices, and the intersection of the 1/2 bit threshold with the FSC curve was used to determine the maximum resolution.

RESULTS

Two Crossed Tubes Phantom

Figure 4 shows a 3D rendering of a single time point of vaporized PCCAs in (A) both tubes, (B) tube 1, and (C) tube 2. Figures 4D–F show a volume rendering of the temporal maximum projection and (G, H, I) the 3D localization density map. In Figure 4J, the separation of the 2 tubes is

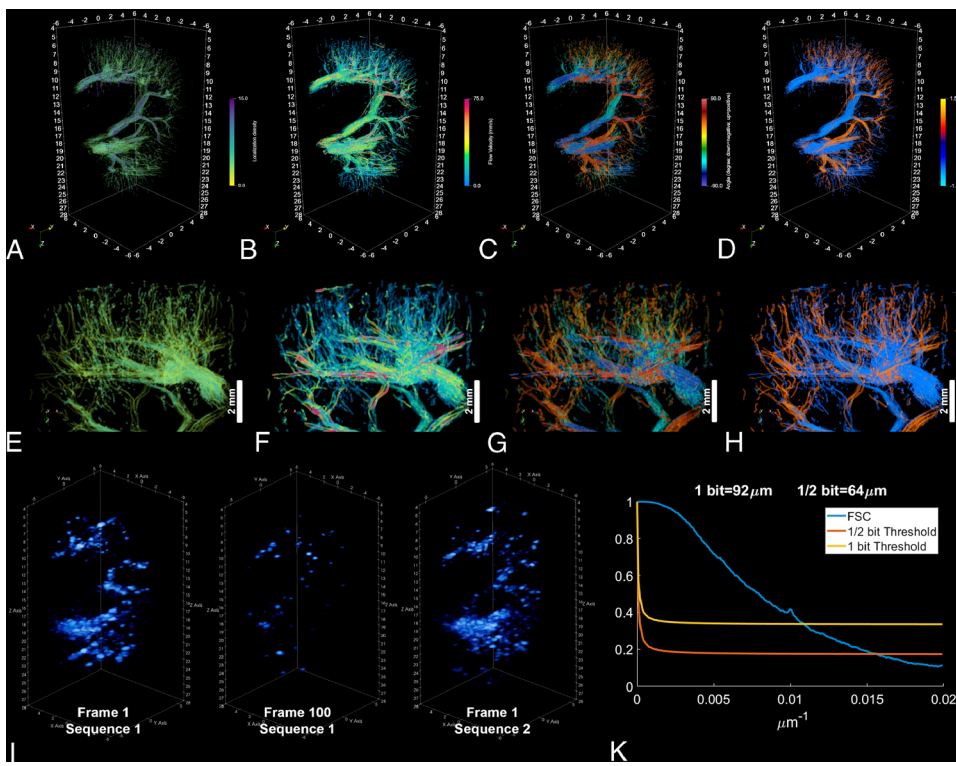

FIGURE 5. Super-resolved vasculature of the rabbit kidney through repeated activation of C_3F_8:C_4F_{10} (3:1) PCCAs at depth of 20 mm. The localization density map (A), velocity magnitude (B), angle (C), and binary direction (D) reconstructed from 1500 frames/8 s of acquisition. The respective zoomed in view of the metric maps (E, F, G, H). Visualization of the repeated activation of PCCAs in the kidney through single time points of the first and second sequence (I). Spatial resolution based on the FSC criterion 92 μm/64 μm (K), which demonstrated the resolution improvement of up to 9-fold compared with the PSF and 1.5-fold compared with half the wavelength. The white bar is 2 mm long (E–H).

presented by plotting the localization density at their closest point. The profile was averaged over the width illustrated by the white box along a manually selected line. The theoretical distance between the 2 cellulose tubes was 300 µm. The number of focus regions was changed for the different examples indicated by the green rectangles. The focus was set at 15/12/15 mm with 16/4/8 repeated transmissions for element position 8–24/8–24/16 (X-direction) and using all/all/16 rows in Y-direction (A/B/C). As a consequence, the localization density was lower in the individually activated tubes that had fewer focus points targeted at them as shown by the green rectangles.

Renal Vasculature of Rabbit

The super-resolved vasculature, flow magnitude, angle (relative to Z-direction), and binary flow direction (distal or proximal) of a rabbit's kidney can be seen in Figures 5A–D, respectively. This demonstrated the ability of 3D AWSALM to activate PCCAs in vivo. A close-up view of each image is shown in (E–H). The activation focus was set at 20 mm with 15 repeated transmissions using element position 8–24 in the X-direction and using all elements in Y-direction. The localization density map and the 15 repeated activations of PCCAs can also be viewed in the Supplementary Video 1, http://links.lww.com/RLI/A870, and in Figure 5I. The PCCA density is highest immediately after the activation sequence, and the number of activated PCCAs in the field of view falls off over the 100 frames acquired. The spatial resolution was measured to be 64 µm for the 1/2 bit FSC threshold criterion. This is a resolution improvement of more than 9-fold compared with the measured size of the PSF and 1.5 times compared with Abbe's (half wavelength, 96.25 µm) diffraction limit.

Selective Activation of the Renal Vasculature

Figure 6 demonstrates the 3D AWSALM's ability to selectively activate PCCAs in 3D space for 2 different rabbit kidneys. Figures 6A–H show an instance of PCCA activation (A, E) on the left (green) or right side (yellow), the respective binary direction maps of the vasculature (B, F) and (C, G) of the left kidney, and their combined results (D, H). Figures 6I–L show the results of activating PCCAs (I) close to the ultrasound probe (green) or at depth (yellow), the respective microvasculature and macrovasculature (J, K) direction maps. The combined result can be

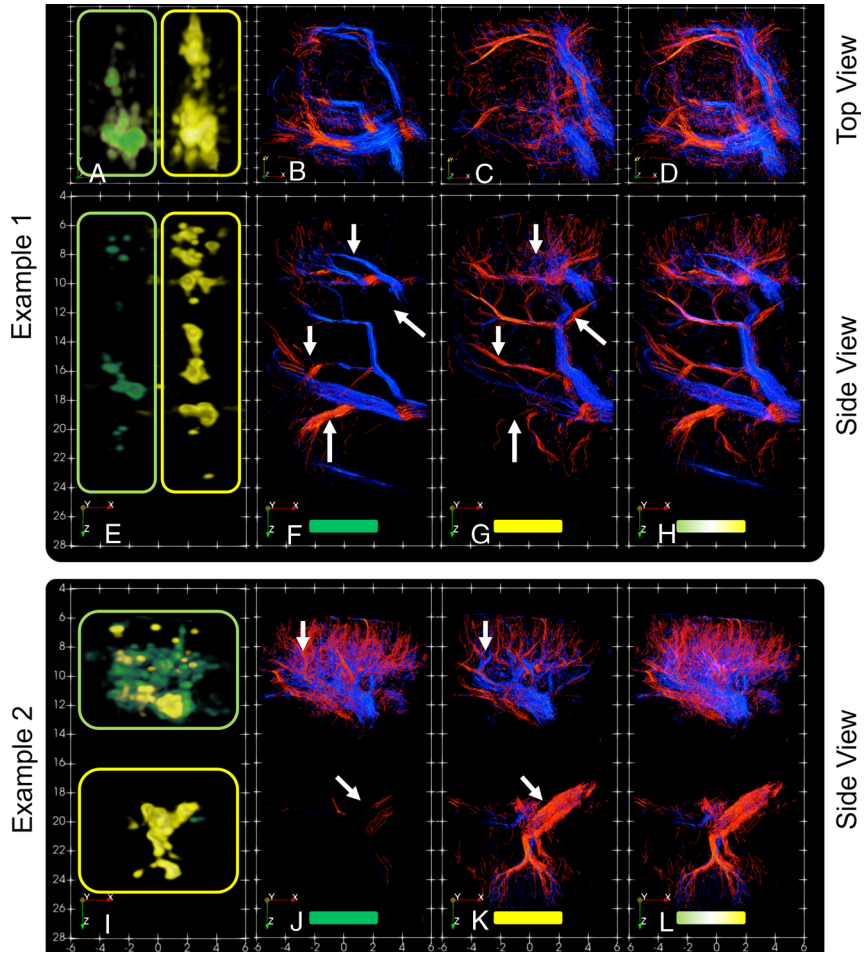

FIGURE 6. Selective activation of C_3F_8:C_4F_{10} (3:1) PCCAs in 3 dimensions from 2 different examples in 2 different rabbits. Example 1 compares the activation on the left or on the right side of the field of view each marked by either green or yellow. Example 2 compares the activation of PCCAs at a shallow and a deep depth also marked by green or yellow. The activation frame of each setting is combined into a single view (A, E, I). All other images show the binary direction map with red indicating upward flow and blue downward flow. Images (A–D) show the top and (E–H) the side view of example 1, and for example 2, only the side view of a different animal and from a different acquisition is presented (I–L). Activation frame (A, E), binary direction map on the left (B, F), the right (C, G), and combined (D, H). Activation frame (I), binary direction map at a shallow depth (J), at deeper depth (K), and combined (L). The white arrows mark vessels that are not visualized in their respective counterpart and make vascular connections visible, which is otherwise difficult to detect.

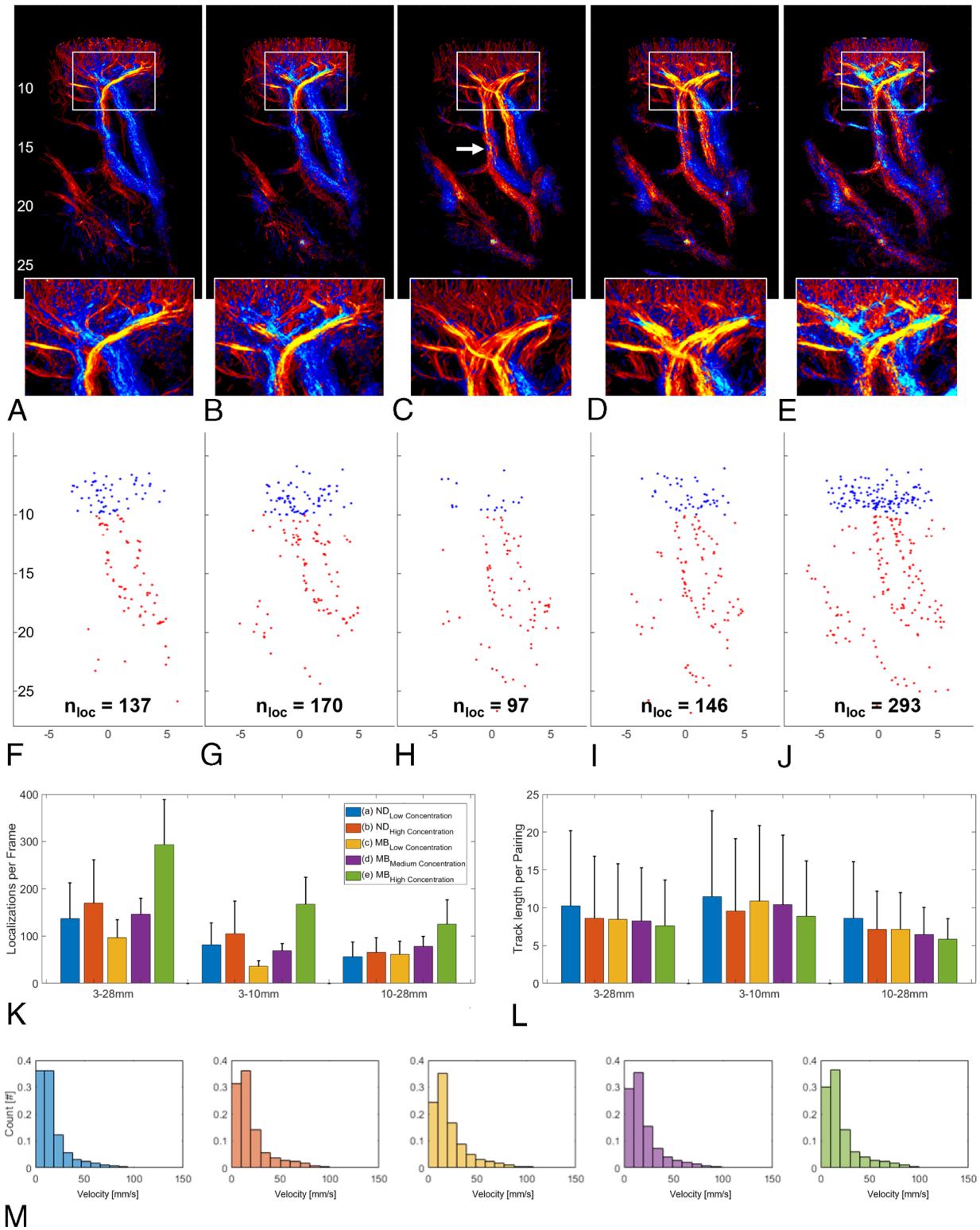

FIGURE 7. Comparison of 3D AWSALM and MB-based ULM localization density-weighted direction maps with (A) low ND, (B) high ND, (C) low MB, (D) medium MB, and (E) high MB concentrations. For each map, a zoomed in ROI is shown. Representative localization frame with color-coded localizations circles for each acquisition (first frame where the number of localizations is equal to the mean number of localizations, blue indicating microvasculature and red macrovasculature). K, Average localization events per frame for 3 different depth ranges (all: 3–28 mm, microvasculature: 3–10 mm, macrovasculature: 10–28 mm) and (L) average track lengths (number of pairings) as a function of depth in the image. M, Histogram of velocities for depth range 3–10 mm. The depth definition of the microvasculature and macrovasculature was selected manually. The focus was set at a depth of 20 mm with 15 repeated transmissions.

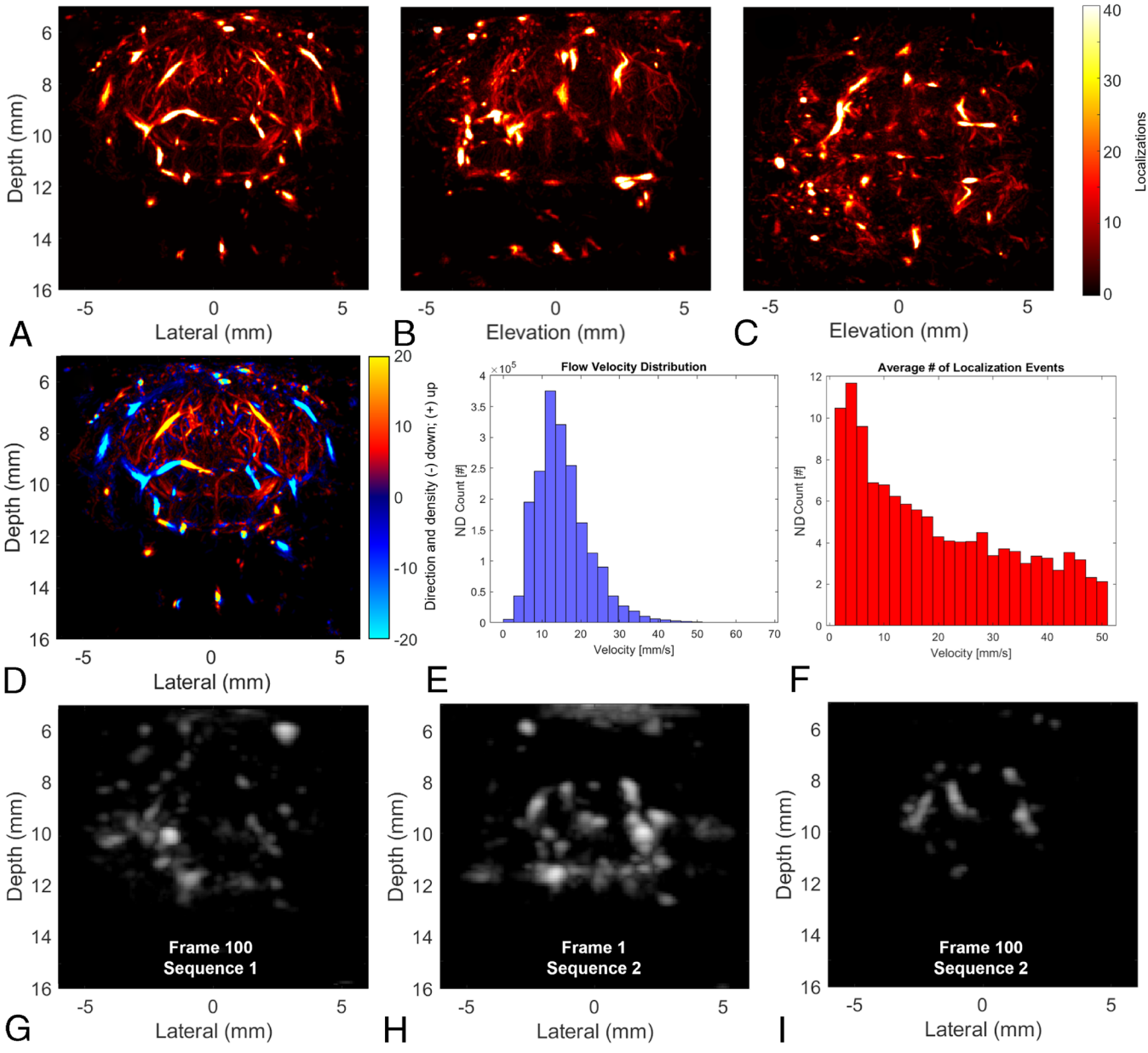

FIGURE 8. Transcranial 3D AWSALM of the mouse brain vasculature with localization density maps in a coronal (A), sagittal (B), and top (D) view. Focused activation at 10 mm depth. Density map of a representative mice brain in a coronal (i), sagittal (ii), and top (iii) view using C_3F_8:C_4F_{10} (4:1) PCCAs and a total of 15,000 frames/80 s of acquisition. E, Localization weighted binary direction map, histogram of flow velocities (C), and histogram of PCCA count as a function of flow velocities (F). Illustration of the repeated activation of PCCAs through the skull (G–I).

seen in (L). Supplementary Video 2, http://links.lww.com/RLI/A871, shows 15 repeated activations when activating the left or right side of the first example of a left rabbit kidney (A–H). Selectivity is distinct when activating at different X-Y coordinates (A, E). Activation at depth also activated some PCCAs in the microvasculature, but no PCCAs were activated when focusing close to the probe (I, M). The focus was set at 15/15/12/20 mm with 15/15/15/15 repeated transmissions for element position 8/24/8–24/8–24 (X-direction) and using all elements in Y-direction (B/C/J/K).

Comparison Between 3D MB ULM and 3D AWSALM

Figure 7 demonstrates the increased vascular perfusion of PCCAs while retaining sparsity in larger vessels and the limitations of the selective activation. The focus was set at a depth of 20 mm with 15 repeated transmissions between element position 8 and 24 (X-direction) and using all elements in Y-direction. The localization density-weighted direction map of an acquisition with low (A) and high (B) PCCA concentration and of low (C), medium (D), and high (E) MB concentration is shown. Localization events of the first frame that contains an average number of localizations (n_{loc}) are mapped for each setting respectively below (F–J). Localizations are color coded based on depth, where blue represents microvasculature (3–10 mm) and red macrovasculature (10–28 mm). Mean localization events per frame (K) and average track lengths (number of pairings; not distance) for each of the 5 cases (L), and the histogram of velocities between 3 and 10 mm depth (M) are presented. Phase change contrast agent had a higher count in the microvasculature

than in the macrovasculature for both concentrations, whereas MBs behaved in the opposite for low and medium concentrations but not for the high concentration (A–J, K). With similar numbers of localizations in the macrovasculature (10–28 mm), PCCA had a higher number of localizations in the microvasculature (B, C, K). The average track lengths (L) was overall highest for the lowest PCCA concentration. Increasing MB saturation increased the localization count in the microvasculature (highest overall) at the cost of track length (K, L, M). Figure 7E illustrates that the decrease in track length was accompanied by tracking errors. This shows qualitatively by a direction map that is locally less homogeneous (zoomed in ROI in A–E). With a low MB concentration, the flow in the microvasculature is almost exclusively in upward direction but not for a high MB concentration or when using PCCAs. In Supplementary Video 3, http://links.lww.com/RLI/A872, the signal of MBs in the large vessel is a fully developed speckle, but the PCCA signal remains sparse. The white arrow (C) marks a large upward flowing branch not seen with PCCAs.

Feasibility of Transcranial Imaging of a Mouse Brain

Figure 8 and Supplementary Video 4, http://links.lww.com/RLI/A873, illustrate the feasibility of 3D AWSALM in a mouse brain. By using easy to vaporize PCCAs, 3D AWSALM can activate transcranial as shown in Figures 8G, H, and I. The focus was set at a depth of 10 mm with 15 repeated transmissions between element position 8–24 (X-direction) and using all elements in Y-direction. The localization density map of the mouse brain is shown in a coronal (A), sagittal (B), and top (C) view, and the localization weighted binary direction map is illustrated in (D). The cerebral flow distribution peaked between 12.5 and 15 mm/s (E) with a higher PCCA count for lower flow velocities (F). After acoustic activation, PCCAs appear bigger and brighter compared with when they spontaneously vaporize.

DISCUSSION

In this work, we demonstrated 3D AWSALM that combines subdiffraction limit imaging with spatiotemporal selectivity and enhanced microvascular penetration. By using gas mixture PCCAs, we were able to image, validate, and present the feasibility of 3D AWSALM in 2 crossed tubes, the kidney of NZW rabbits and the brain of C57BL/6J mice. The activation of PCCAs could be broad or selective, with the latter making vascular connections visible without further processing. Three-dimensional ULM has already been shown capable of discriminating between ischemic and hemorrhagic stroke.[26] Three-dimensional AWSALM may add additional value by being able to detect vascular connectivity, for example, collateral vasculature that serves as a natural bypass in response to reduced or blocked blood flow,[32] and by being able to follow the flow from the source to the peripheral vasculature. The comparison between MB-based ULM and 3D AWSALM demonstrated that, with a similar count in the macrovasculature, more localizations were made in the microvasculature and the observed tracks were on average longer. The transcranial 3D AWSALM demonstrated that PCCA can be acoustically activated behind the skull with pressures well within recommended safety limits. Finally, the demonstration of AWSALM in 3D has overcome a key limitation of our previous work of only being able to activate PCCAs in a plane.[21]

Recent studies have already demonstrated impressive detail obtained through the high spatiotemporal resolution of MB-based 3D ULM when it is used for deep vascular imaging, including of the heart and through the skull.[24,25,27,33] These studies show superior super-resolution image quality, but at the cost of acquisition times of several minutes. Super-resolution image quality is strongly dependent upon acquisition time and MB concentration, and hence is challenging to improve. Strategies such as MB uncoupling, MB separation, or improved beamforming have been trialed with success[34–36] but are still restricted by the limitations of using MBs. By increasing the frequency at which PCCAs are activated in the microcirculation, the acquisition time could be reduced. Another advantage with 3D AWSALM is that the selective contrast activation of only a partial segment of the vasculature of interest is possible. This can help minimize nonlinear propagation artifacts[15,16] and allows vascular connectivity to be investigated. Three-dimensional AWSALM has the potential to detect the presence of collateral vessels.[37,38] The main disadvantage of 3D AWSALM over 3D MB-based ULM is that currently clinically approved PCCAs do not exist. This makes the translation to clinic difficult and expensive.[39] Another consideration is the biocompatibility of PCCAs and their biological safety.[40,41] Phase change contrast agents can extravasate, so they are not confined by the blood space.[42,43] Furthermore, vaporization in small vessels, for example, in the brain, may itself cause harm; this needs to be further investigated. Moreover, Figure 7 illustrates another potential disadvantage: the difficulty of selective activation of PCCAs in the appropriate imaging region. Activation is subject to the diffraction limit and may exceed the vaporization threshold in nonfocal regions nearby; isolation of a vessel is simpler in X-Y plane than in Z-direction (Fig. 5). Spatially varying tissue attenuation causes inhomogeneity in the activation field and can interfere with PCCA activation. Activation of PCCA is linearly related to the PCCA concentration,[29] is a function of the peak negative pressure,[44] and may be related to the hydrostatic pressure or surrounding tissue[45,46] and the activation frequency.[47] The optimum fraction of NDs that undergo conversion in the insonated area may need to be determined empirically. The inhomogeneity, the compromise between stability of PCCA and vaporization threshold, and a focused ultrasound transmission all increase the complexity of 3D AWSALM. A final practical complexity is that 3D AWSALM requires activation of the contrast agent. Some a priori knowledge of blood vessel positions is needed to target the activation pulse. This, for example, can be done with tissue harmonic imaging or preinjection power Doppler to guide the activation. As with most super-resolution techniques, a free-hand scanning operator may require extra training to limit hand motion so as not to lose orientation and position.

Nevertheless, selective activation can provide benefits beyond simple MB-based ULM functional parameters. The relationship between the vessels in Figure 6 is clear without further processing. Thus, 3D AWSALM could be used to detect myocardial occlusions[10] or during acute ischemic stroke in addition to current clinical imaging.[48] The most feasible path to clinical approval, however, is likely to be through combining 3D AWSALM with novel therapeutic methods[49] and in applications that already combine imaging and therapeutics.[50,51] Figure 4 demonstrates activation of PCCAs in both tubes and 1 tube at a time. It can also be tuned through the composition of the ultrasound beam or the PCCA themselves. The number of vaporized PCCAs with each transmission is affected by the gas mixture. Our fabrication method for C_3F_8:C_4F_{10} low-boiling-point fluorocarbon phase-change PCCAs has provided the means for AWSALM in 3 dimensions. Further development of PCCAs for imaging such as BANDs[52] will make 3D AWSALM more versatile.

Three-dimensional AWSALM improved spatial resolution over 9-fold (Fig. 4) compared with the PSF, and 1.5-fold compared with the diffraction limit and was comparable to the improvement provided by MB-based ULM. This improvement in resolution is achieved despite the dependence of the FSC method on the vascular saturation in super-resolution images.[31] In addition, Figure 7 demonstrated that using PCCAs rather than MBs gives higher localization counts and longer average track lengths in the microvasculature despite comparable concentrations. There are several limitations to this comparison. Datasets were selected manually to match number of localizations; data processing was identical and not optimized for either, and the standard deviation of the localization count was high. We did not change the repetition frequency at which PCCAs were activated, and we did not match the concentrations of the contrast agents but relied on the surrogate using the number of localizations. Furthermore, the vaporization threshold increases as the size of the droplet decreases.[42] It is therefore

possible that the size distribution of activated PCCAs may be different from that of the MBs and should be further studied. Comparison of 3D AWSALM with 3D ULM is difficult to perform fairly. Ultrasound localization microscopy processing is multistep, with a high number of parameters that need to be tuned appropriately. This could also explain the differences observed between PCCAs and MBs. Arterial flow (upward flowing vessel) is visible in the MB acquisition, but PCCAs were not activated in this vessel Figures 7A and B. Similar observations can be made for vessels on the bottom left of this figure, which skews the comparison of MB activations in microvasculature compared with macrovessels based on the localization count. However, although with MB microvascular saturation is a function of the blood flow (higher during systole), it is also a function of activations for PCCAs (Supplementary Video 3, http://links.lww.com/RLI/A872). The relative count of slow flow (surrogate of the microvasculature) is highest with a low concentration of PCCAs (Fig. 6M). Although the arterial flow may skew the localization count in the macrovasculature, it increases the microvasculature saturation. The PCCA acquisition have higher microvascular localization counts despite a lack of localization in the arterial flow region. The ability of PCCAs to saturate the microvasculature localization count faster than with MBs is further supported by Figure 6. Activation close to the probe revealed a much denser network of vessels. The number of activated PCCAs also changed with the number of focal regions. The large tube (Figures 4A, D, G) had double the localization density when activating the entire ROI compared with when activating only the large tube as shown in Figures 4B, E, H.

Imaging through the skull remains difficult with ultrasound. We demonstrated the feasibility of transcranial 3D AWSALM with a histogram of velocities in good agreement with the literature.[24] We did so with a simple imaging setup that only requires 256 elements in reception. However, more work is necessary to match MB-based transcranial ULM. This includes a higher number of activations and longer acquisition times. Moreover, the vaporization of PCCAs was inhomogeneous. The majority of activated PCCAs were located near the skull and in anterior position.

In this work, we demonstrated the feasibility of 3D AWSALM with acoustically activatable perfluorocarbon PCCAs. Three-dimensional AWSALM can provide contrast on demand, visualize vascular connectivity, take advantage of the accelerated PCCA perfusion of capillaries, and improve the spatial resolution beyond the diffraction limit. The activation can be broad or local and requires acoustics pressures well below recommended safety limits.

REFERENCES

1. Christensen-Jeffries K, Couture O, Dayton PA, et al. Super-resolution ultrasound imaging. *Ultrasound Med Biol*. 2020;46:865–891.
2. Errico C, Pierre J, Pezet S, et al. Ultrafast ultrasound localization microscopy for deep super-resolution vascular imaging. *Nature*. 2015;527:499–502.
3. Christensen-Jeffries K, Browning RJ, Tang M, et al. In vivo acoustic super-resolution and super-resolved velocity mapping using microbubbles. *IEEE Trans Med Imaging*. 2015;34:433–440. Available at: https://ieeexplore.ieee.org/document/6908009.
4. Dewey M, Siebes M, Kachelrieß M, et al. Clinical quantitative cardiac imaging for the assessment of myocardial ischaemia. *Nat Rev Cardiol*. 2020;17:427–450.
5. Kierski TM, Dayton PA. Perspectives on high resolution microvascular imaging with contrast ultrasound. *Appl Phys Lett*. 2020;116:210501.
6. Demené C, Robin J, Dizeux A, et al. Transcranial ultrafast ultrasound localization microscopy of brain vasculature in patients. *Nat Biomed Eng*. 2021;5:219–228.
7. Zhang G, Lei Y-M, Li N, et al. Ultrasound super-resolution imaging for differential diagnosis of breast masses. *Front Oncol*. 2022;12(November):1–11. Available at: https://www.frontiersin.org/articles/10.3389/fonc.2022.1049991/full.
8. Qian X, Kang H, Li R, et al. In vivo visualization of eye vasculature using super-resolution ultrasound microvessel imaging. *IEEE Trans Biomed Eng*. 2020;67:2870–2880. Available at: https://ieeexplore.ieee.org/document/8988233/.
9. Renaudin N, Demené C, Dizeux A, et al. Functional ultrasound localization microscopy reveals brain-wide neurovascular activity on a microscopic scale. *Nat Methods*. 2022;19:1004–1012. Available at: https://www.nature.com/articles/s41592-022-01549-5.
10. Yan J, Huang B, Tonko J, et al. Transthoracic super-resolution ultrasound localisation microscopy of myocardial vasculature in patients. 2023. Available at: http://arxiv.org/abs/2303.14003.
11. Zhu J, Rowland EM, Harput S, et al. 3D super-resolution US imaging of rabbit lymph node vasculature in vivo by using microbubbles. *Radiology*. 2019;291:642–650.
12. Lowerison MR, Sekaran NVC, Zhang W, et al. Aging-related cerebral microvascular changes visualized using ultrasound localization microscopy in the living mouse. *Sci Rep*. 2022;12:619.
13. Ma H, Yang Y, Gao M, et al. A novel rat model of cerebral small vessel disease and evaluation by super-resolution ultrasound imaging. *J Neurosci Methods*. 2022;379:109673.
14. Kanoulas E, Butler M, Rowley C, et al. Super-resolution contrast-enhanced ultrasound methodology for the identification of in vivo vascular dynamics in 2D. *Invest Radiol*. 2019;54:500–516. Available at: http://journals.lww.com/00004424-201908000-00008.
15. Tang M-X, Loughran J, Stride E, et al. Effect of bubble shell nonlinearity on ultrasound nonlinear propagation through microbubble populations. *J Acoust Soc Am*. 2011;129:EL76–EL82.
16. Yildiz YO, Eckersley RJ, Senior R, et al. Correction of non-linear propagation artifact in contrast-enhanced ultrasound imaging of carotid arteries: methods and in vitro evaluation. *Ultrasound Med Biol*. 2015;41:1938–1947. Available at: https://linkinghub.elsevier.com/retrieve/pii/S0301562915002276.
17. Hingot V, Errico C, Heiles B, et al. Microvascular flow dictates the compromise between spatial resolution and acquisition time in ultrasound localization microscopy. *Sci Rep*. 2019;9:2456.
18. Kim J, DeRuiter RM, Goel L, et al. A comparison of sonothrombolysis in aged clots between low-boiling-point phase-change nanodroplets and microbubbles of the same composition. *Ultrasound Med Biol*. 2020;46:3059–3068. Available at: https://linkinghub.elsevier.com/retrieve/pii/S0301562920303008.
19. Sheeran PS, Rojas JD, Puett C, et al. Contrast-enhanced ultrasound imaging and in vivo circulatory kinetics with low-boiling-point nanoscale phase-change perfluorocarbon agents. *Ultrasound Med Biol*. 2015;41:814–831. Available at: https://linkinghub.elsevier.com/retrieve/pii/S0301562914007108.
20. Durham PG, Dayton PA. Applications of sub-micron low-boiling point phase change contrast agents for ultrasound imaging and therapy. *Curr Opin Colloid Interface Sci*. 2021;56:101498.
21. Riemer K, Toulemonde M, Yan J, et al. Fast and selective super-resolution ultrasound in vivo with acoustically activated nanodroplets. *IEEE Trans Med Imaging*. 2023;42:1056–1067. Available at: https://ieeexplore.ieee.org/document/9955557/.
22. Zhang G, Harput S, Lin S, et al. Acoustic wave sparsely activated localization microscopy (AWSALM): super-resolution ultrasound imaging using acoustic activation and deactivation of nanodroplets. *Appl Phys Lett*. 2018;113.
23. Lin F, Shelton SE, Espíndola D, et al. 3-D ultrasound localization microscopy for identifying microvascular morphology features of tumor angiogenesis at a resolution beyond the diffraction limit of conventional ultrasound. *Theranostics*. 2017;7:196–204. Available at: http://www.thno.org/v07p0196.htm.
24. Demeulenaere O, Bertolo A, Pezet S, et al. In vivo whole brain microvascular imaging in mice using transcranial 3D ultrasound localization microscopy. *EBioMedicine*. 2022;79:103995. Available at: https://linkinghub.elsevier.com/retrieve/pii/S2352396422001797.
25. Demeulenaere O, Sandoval Z, Mateo P, et al. Coronary flow assessment using 3-dimensional ultrafast ultrasound localization microscopy. *JACC Cardiovasc Imaging*. 2022;15:1193–1208.
26. Chavignon A, Hingot V, Orset C, et al. 3D transcranial ultrasound localization microscopy for discrimination between ischemic and hemorrhagic stroke in early phase. *Sci Rep*. 2022;12:14607.
27. McCall JR, Santibanez F, Belgharbi H, et al. Non-invasive transcranial volumetric ultrasound localization microscopy of the rat brain with continuous, high volume-rate acquisition. *Theranostics*. 2023;13:1235–1246. Available at: https://www.thno.org/v13p1235.htm.
28. Mountford PA, Smith WS, Borden MA. Fluorocarbon nanodrops as acoustic temperature probes. *Langmuir*. 2015;31:10656–10663.
29. Li S, Lin S, Cheng Y, et al. Quantifying activation of perfluorocarbon-based phase-change contrast agents using simultaneous acoustic and optical observation. *Ultrasound Med Biol*. 2015;41:1422–1431.
30. Yan J, Zhang T, Broughton-Venner J, et al. Super-resolution ultrasound through sparsity-based deconvolution and multi-feature tracking. *IEEE Trans Med Imaging*. 2022;41:1938–1947.
31. Hingot V, Chavignon A, Heiles B, et al. Measuring image resolution in ultrasound localization microscopy. *IEEE Trans Med Imaging*. 2021;40:3812–3819. Available at: https://ieeexplore.ieee.org/document/9490980/.
32. Perovic T, Harms C, Gerhardt H. Formation and maintenance of the natural bypass vessels of the brain. *Front Cardiovasc Med*. 2022;9(March):1–6. Available at: https://www.frontiersin.org/articles/10.3389/fcvm.2022.778773/full.

33. Chavignon A, Heiles B, Hingot V, et al. 3D transcranial ultrasound localization microscopy in the rat brain with a multiplexed matrix probe. *IEEE Trans Biomed Eng*. 2022;69:2132–2142. Available at: https://ieeexplore.ieee.org/document/9658204/.
34. Huang C, Lowerison MR, Trzasko JD, et al. Short acquisition time super-resolution ultrasound microvessel imaging via microbubble separation. *Sci Rep*. 2020;10:6007.
35. Kim J, Lowerison MR, Sekaran NVC, et al. Improved ultrasound localization microscopy based on microbubble uncoupling via transmit excitation. *IEEE Trans Ultrason Ferroelectr Freq Control*. 2022;69:1041–1052. Available at: https://ieeexplore.ieee.org/document/9684367/.
36. Yan J, Wang B, Riemer K, et al. Fast 3D super-resolution ultrasound with adaptive weight-based beamforming. *IEEE Trans Biomed Eng*. 2023;1–10. Available at: http://arxiv.org/abs/2208.12176.
37. Seiler C. The human coronary collateral circulation. *Heart*. 2003;89:1352–1357. Available at: https://heart.bmj.com/lookup/doi/10.1136/heart.89.11.1352.
38. Meier P, Schirmer SH, Lansky AJ, et al. The collateral circulation of the heart. *BMC Med*. 2013;11:1. Available at: BMC Medicine.
39. Nunn AD. The cost of developing imaging agents for routine clinical use. *Invest Radiol*. 2006;41:206–212. Available at: http://journals.lww.com/00004424-200603000-00002.
40. Fan C-H, Lin Y-T, Ho Y-J, et al. Spatial-temporal cellular bioeffects from acoustic droplet vaporization. *Theranostics*. 2018;8:5731–5743. Available at: http://www.thno.org/v08p5731.htm.
41. Miller DL, Averkiou MA, Brayman AA, et al. Bioeffects considerations for diagnostic ultrasound contrast agents. *J Ultrasound Med*. 2008;27:611–632; quiz 633–6. Available at: http://www.ncbi.nlm.nih.gov/pubmed/18359911.
42. Zullino S, Argenziano M, Stura I, et al. From micro- to nano-multifunctional theranostic platform: effective ultrasound imaging is not just a matter of scale. *Mol Imaging*. 2018;17:153601211877821. Available at: http://journals.sagepub.com/doi/10.1177/1536012118778216.
43. Rojas JD, Dayton PA. In vivo molecular imaging using low-boiling-point phase-change contrast agents: a proof of concept study. *Ultrasound Med Biol*. 2019;45:177–191. Available at: https://linkinghub.elsevier.com/retrieve/pii/S0301562918303545.
44. Mountford PA, Thomas AN, Borden MA. Thermal activation of superheated lipid-coated perfluorocarbon drops. *Langmuir*. 2015;31:4627–4634. Available at: https://pubs.acs.org/doi/10.1021/acs.langmuir.5b00399.
45. Raut S, Khairalseed M, Honari A, et al. Impact of hydrostatic pressure on phase-change contrast agent activation by pulsed ultrasound. *J Acoust Soc Am*. 2019;145:3457–3466. Available at: https://pubs.aip.org/asa/jasa/article/145/6/3457-3466/940271.
46. Rojas JD, Borden MA, Dayton PA. Effect of hydrostatic pressure, boundary constraints and viscosity on the vaporization threshold of low-boiling-point phase-change contrast agents. *Ultrasound Med Biol*. 2019;45:968–979.
47. Sheeran PS, Matsunaga TO, Dayton PA. Phase-transition thresholds and vaporization phenomena for ultrasound phase-change nanoemulsions assessed via high-speed optical microscopy. *Phys Med Biol*. 2013;58:4513–4534. Available at: https://iopscience.iop.org/article/10.1088/0031-9155/58/13/4513.
48. Liu L, Ding J, Leng X, et al. Guidelines for evaluation and management of cerebral collateral circulation in ischaemic stroke 2017. *Stroke Vasc Neurol*. 2018;3:117–130. Available at: https://svn.bmj.com/lookup/doi/10.1136/svn-2017-000135.
49. Lea-Banks H, Wu S-K, Lee H, et al. Ultrasound-triggered oxygen-loaded nanodroplets enhance and monitor cerebral damage from sonodynamic therapy. *Nanotheranostics*. 2022;6:376–387. Available at: https://www.ntno.org/v06p0376.htm.
50. Zhang W, Shi Y, Abd Shukor S, et al. Phase-shift nanodroplets as an emerging sonoresponsive nanomaterial for imaging and drug delivery applications. *Nanoscale*. 2022;14:2943–2965. Available at: http://xlink.rsc.org/?DOI=D1NR07882H.
51. Zhao F, Unnikrishnan S, Herbst EB, et al. A targeted molecular localization imaging method applied to tumor microvasculature. *Invest Radiol*. 2021;56:197–206. Available at: https://journals.lww.com/10.1097/RLI.0000000000000728.
52. Dong F, An J, Zhang J, et al. Blinking acoustic nanodroplets enable fast super-resolution ultrasound imaging. *ACS Nano*. 2021;15:16913–16923. Available at: https://pubs.acs.org/doi/10.1021/acsnano.1c07896.